JOURNAL OF SPACECRAFT AND ROCKETS
Vol. 46, No. 6, November–December 2009

Computational Assessment of Thermal Protection System Damage Experienced During STS-118

Grant E. Palmer*
ELORET Corporation, Sunnyvale, California 94086
Maria Pulsonetti,† William A. Wood,† Steve Alter,† and Peter Gnoffo‡
NASA Langley Research Center, Hampton, Virginia 23681
and
Chun Tang*
NASA Ames Research Center, Moffett Field, California 94035

DOI: 10.2514/1.40478

In response to thermal protection system tile damage that occurred during the ascent portion of space shuttle mission STS-118, rapid turnaround computational fluid dynamic simulations were performed on the damage site during the mission. The purpose of the computational effort was to provide insight into the flow physics and determine heating augmentation bump factors in and around the damage site. Damage analysis teams at the NASA Ames and NASA Langley Research Centers used automated local cavity simulation procedures to generate 12 three-dimensional simulations in less than 18 h during the mission. The computational fluid dynamic results compared closely with the engineering results used as inputs to the vehicle thermal analysis models and supported the recommendation of the damage assessment team to fly the Orbiter back as is without requiring the astronauts to perform a damage site repair in situ.

I. Introduction

IN RESPONSE to the accident of the Space Shuttle *Columbia* in February 2003, a thermal protection system (TPS) damage assessment process was developed following the recommendations of the Columbia Accident Investigation Board (CAIB) report [1,2]. On the ascent portion of the flight, the TPS of the Orbiter is subject to damage due to impacts with ice, detached pieces of insulation, birds, and other causes. A group of analysts known as the Damage Assessment Team (DAT) are charged with the responsibility of evaluating damage sites and making recommendations on whether or not to repair the damage sites to the Orbiter Project Office and Mission Management Team (MMT) review boards.

As part of the damage assessment process, detailed images are taken of the vehicle TPS when the Orbiter reaches the International Space Station (ISS). Damage sites evident in the images are catalogued and those that cannot be closed out based on previous experience are passed on to the DAT for further analysis. For cavity damage sites, simplified representations of the cavity geometry are created that preserve key geometrical aspects of the damage site. The simplified geometries are given to the aerothermodynamics team where engineering-level tools are used to generate heating augmentation bump factors (localized heating rates in and around the cavity scaled by a reference heating rate taken upstream of the cavity). The heating bump factors are provided to the thermal analysis and structures teams, where they are used as inputs to thermal math models that determine the effects of the cavity on the underlying structure of the vehicle.

The heating rate bump factors used in the thermal model for trapezoidal, shoebox-shaped cavities are primarily obtained from the NASA/Boeing Cavity Heating Tool (CHT) [3], which uses correlations derived from experimental data. The CHT has been certified for shoebox cavities, trapezoidal-shaped cavities that can have sloped side and end walls. If the cavity shapes deviate sufficiently from the shoebox geometry, higher-fidelity computational fluid dynamic (CFD) analysis is performed to determine the heating augmentation bump factors. CFD solutions may also be generated for standard shoebox cavities to compare against the engineering-level results.

During the STS-118 mission in August 2007, a piece of foam insulation was released from the external tank of the Space Shuttle *Endeavour* during the vehicle ascent. The foam struck the TPS tiles toward the aft end of the windward surface of the vehicle, as shown in Fig. 1. The impact caused a 3-in.-long by 2-in.-wide (0.076 m by 0.051 m) cavity that was designated as damage site D-118-RPM-600_2-001. A focused inspection of the damage site performed when the Orbiter was docked to the space station produced the photograph shown in Fig. 2. As can be seen in the picture, a section of the cavity appeared to penetrate all the way through the TPS tile exposing a section of the thin, feltlike insulating layer known as the filler bar. The concern was that the filler bar might not prove sufficient in preventing the heat of the external flow during reentry from soaking into the aluminum structure of the vehicle.

As part of STS-118 DAT analysis, scientists at the NASA Ames and NASA Langley Research Centers were asked to perform detailed 3-D CFD computations of damage site D-118-RPM-600_2-001. The objective of the CFD analysis was to provide insight into the flow structures and flow physics in the interior of the cavity and to predict the heating augmentation bump factors for comparison against those predicted by the certified engineering tools. Arcjet tests and associated CFD simulations were also performed during the mission but are beyond the scope of this paper.

Presented as Paper 4246 at the 40th AIAA Thermophysics Conference, Seattle, WA, 23–26 June 2008; received 18 August 2008; revision received 3 August 2009; accepted for publication 4 August 2009.

*Senior Research Scientist, Reacting Flow Environments Branch, Mail Stop 230-2. Associate Fellow AIAA.
†Senior Research Scientist, Aerothermodynamics Branch, Mail Stop 408-A. Senior Member AIAA.
‡Senior Research Scientist, Aerothermodynamics Branch, Mail Stop 408-A. Fellow AIAA.

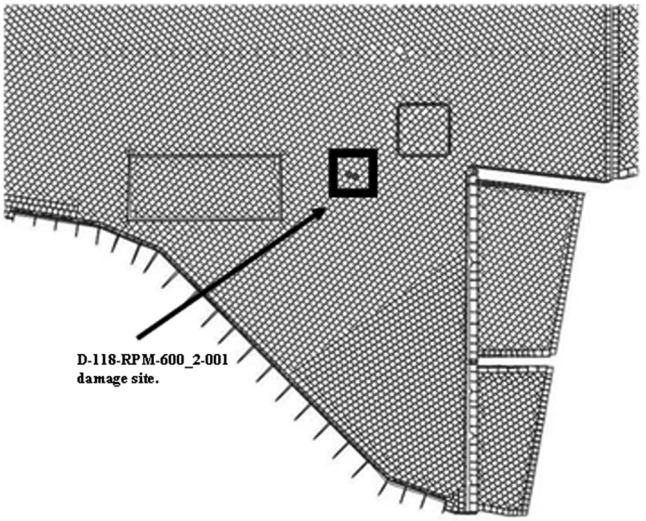

Fig. 1 Location of D-118-RPM-600_2-001 damage site.

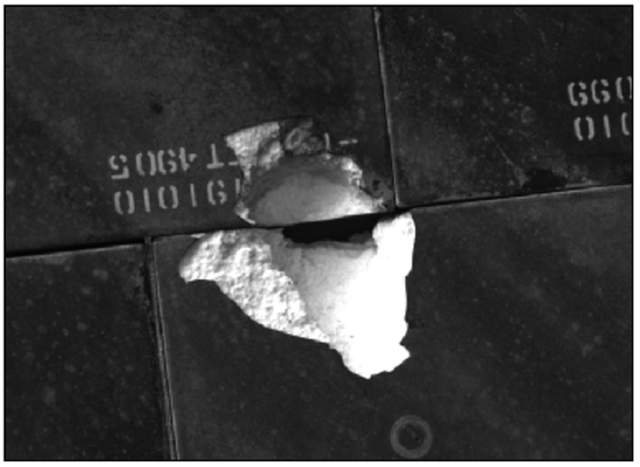

Fig. 2 On-orbit photograph of damage site D-118-RPM-600_2-001.

II. Local Cavity Computational Fluid Dynamic Procedures

In response to a recommendation from the CAIB report to "develop, validate, and maintain physics-based computer models to evaluate TPS damage from debris impacts" [1], the aeroheating CFD teams at Langley and Ames developed rapid-analysis procedures for generating same-day high-fidelity CFD cavity solutions during shuttle mission support [4–6]. The CFD processes have been validated against wind-tunnel experimental data [6]. A complete description of the Ames and Langley rapid-analysis procedure can be found in [4–6]. A brief summary of the procedures is provided here.

A simplified representation of the cavity damage site geometry is generated from the detailed imagery. A local system of 3-D grid blocks is constructed over and inside the damage site for each selected flight condition. The local grid generation and flow initialization are performed using automated scripts that require minimal user input to execute. The Ames procedure uses what is known as a glyph script from the Gridgen commercial grid generation software [7]. Surface patches are grown hyperbolically outward from the cavity edges. The corresponding volume grid blocks are constructed one radial line at a time at each grid layer off the surface. A cell-centered flow starting guess is interpolated similarly, including at the outer boundary where the inflow conditions define the local problem. The block(s) in the cavity are initialized by interpolation within the surface patch(es) above the cavity. A virtue of the Ames cavity analysis procedure is that, even though a special-purpose surface grid and three-block volume grid inside the cavity had to be prepared

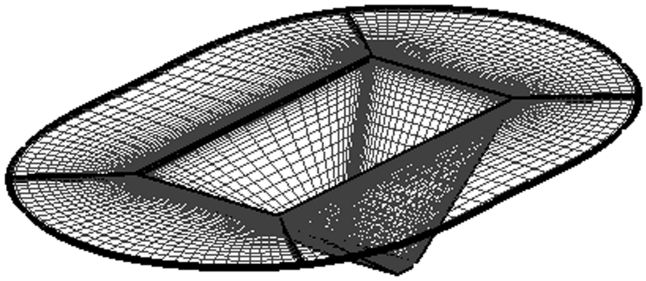

Fig. 3 A typical local system of surface grids generated over a cavity damage site (Ames procedure).

interactively for the D-118-RPM-600_2-001 damage site because of the floor irregularity, the rest of the automated scheme (for main volume gridding and flow initialization) remained perfectly applicable. The Langley procedure proceeds along similar lines. It uses an in-house grid-morphing utility named MORPH that creates local cavity grid blocks that connect smoothly into the smooth outer mold line (OML) baseline grids and interpolates a starting solution onto the local grid. A typical local cavity system of surface patches from the Ames procedure is shown in Fig. 3. The solutions on the local cavity grids are then computed using either the data-parallel line relaxation (DPLR) [8] or the Langley aerothermodynamic upwind relaxation algorithm (LAURA) [9] CFD flow solvers. The DPLR and LAURA codes are the NASA standards for computing reacting gas CFD solutions around the Orbiter [2,10,11]. Typically, the local cavity solutions are computed on the NASA advanced supercomputing (NAS) Columbia supercomputer cluster at NASA Ames.

As part of the shuttle Return to Flight program, a database of 44 laminar and 6 turbulent smooth-OML CFD solutions has been generated at Mach numbers ranging from 25 down to 6 along the STS-107, STS-115, and ISS heavy vehicle forward weight trajectories. These CFD solutions are stored in a repository maintained by NAS. Data from the smooth-OML solutions are interpolated onto the local cavity grids as a starting solution.

For the STS-118 damage assessment, local cavity CFD solutions were generated at five trajectory points spanning the key range of interest in the laminar part of the entry trajectory. The freestream values for these CFD points are listed in Table 1. The smooth-OML solutions were chosen based on the closest match to the STS-118 trajectory. The Mach 25 trajectory point on the STS-118 trajectory was closest to the STS-115 database point, whereas the other STS-118 points were closer to the STS-107 smooth-OML conditions. A five-species (N, O, N_2, O_2, NO), one-temperature air chemistry model was used to model real-gas effects. The surfaces in and around the cavity were assumed to be in radiative equilibrium with the external flow. The model used reaction-cured glass surface kinetics. The reference heating values in Table 1 are Fay–Riddell stagnation point values [12].

III. Simplified Cavity Geometries

The shape and dimensions of cavity D-118-RPM-600_2-001 were determined during a focused inspection performed when the Space Shuttle *Endeavour* was docked to the ISS. Data from the laser camera system (LCS) were used to create a point-cloud model representing the interior of the cavity, as shown in Fig. 4. As seen in the point-cloud representation, the interior of the cavity is irregularly shaped. The shape can be roughly approximated to a cavity within a cavity with a larger, trapezoidal cavity sitting on top of a smaller cavity. The bottom of the smaller cavity was where the filler bar was exposed. Postflight analysis indicated that there was a 1.5% error in the volume estimate generated from the LCS data compared with the actual cavity volume.

The CHT, the certified engineering tool used to compute the heating augmentation bump factors used in the thermal analysis models, was not designed to simulate the complicated shape of the D-118-RPM-600_2-001 cavity. CFD grids, on the other hand, could be constructed to model the damage site more accurately, but to do so

Table 1 Freestream conditions for D-118-RPM-600_2-001 cavity CFD runs

Mach	Trajectory	Density, kg/m^3	Velocity, m/s	Temperature, K	α, deg	Ref. heating, W/cm^2
25	STS-115	4.5943e − 5	7187.4	207.7	40	46.7
23	STS-107	7.9976e − 5	6859.5	223.0	40	51.8
20	STS-107	1.3453e − 4	6160.1	229.1	42	47.8
18	STS-107	2.6099e − 4	5536.5	238.5	39	47.1
16.5	STS-107	3.3177e − 4	5081.1	242.6	40	41.6

would require the cavity grids to be generated manually, a time-consuming process that was impractical in view of the urgency of the bump factor analysis. Performing an in-space repair requires extensive planning for the extravehicular activity (EVA). Therefore, the CFD analysis had to be completed in 18 h to be useful in the decision-making process. Because of the time constraints, three simplified cavity geometries were developed that captured the key dimensions and wall angles of the actual cavity, yet could be modeled using the rapid-analysis techniques. The shapes of the simplified cavities were not driven solely, or even primarily, by CFD considerations, but rather because they were shapes that could be incorporated into the thermal and structural analysis models.

The standard local cavity grid generation techniques developed at NASA Ames and Langley Research Centers are designed to model trapezoidal shoebox cavities. The first simplified cavity shape, known as simplified cavity 2 and seen in Fig. 5a, models a simple, trapezoidal, sloped-wall representation of the D-118-RPM-600_2-001 cavity that preserved the overall volume of the cavity and the length of the exposed filler-bar region. The second simplified cavity geometry, known as simplified cavity 3 and shown in Fig. 5b, captures the cavity within a cavity nature of the actual damage site by representing the cavity as a larger trapezoidal shoebox cavity on top of a smaller one. Instead of the flat, constant-slope backwall of simplified cavity 2, the aft section of simplified cavity 3 models the relatively flat backshelf area seen in the actual damage site. The exposed filler-bar length in both simplified cavities is 0.2 in. or 0.00508 m. The height of simplified cavity 2 is 1.1 in. (0.0279 m), whereas the overall height of simplified cavity 3 is 1.13 in. (0.0287 m).

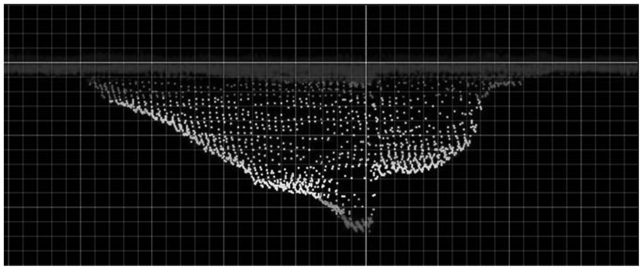

Fig. 4 Point cloud of the D-118-RPM-600_2-001 cavity.

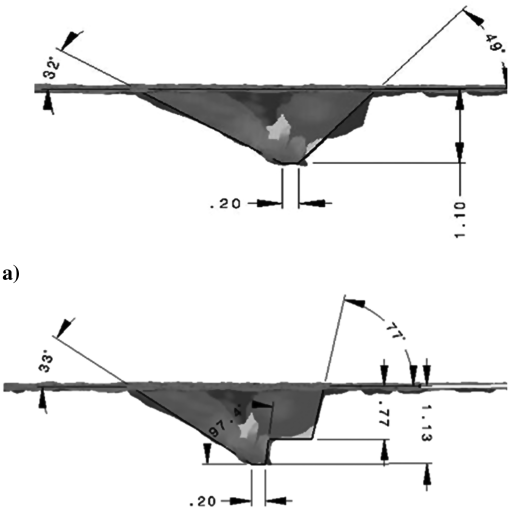

Fig. 5 Simplified cavity geometries: a) simplified cavity 2, and b) simplified cavity 3.

The CHT can be directly applied to simplified cavity 2, because it represents a standard, shoebox cavity shape. The CHT can be (and was) applied to simplified cavity 3 by considering the cavity shape to be a cavity within a cavity. The CHT was run twice with the bump factors in the gap-filler region obtained from the product of the bump factors from the two CHT runs. This approach is conceptually straightforward, but the CHT has not been certified for a simplified cavity 3 geometry, which was one reason CFD was brought into the damage assessment process.

An alternative cavity geometry was developed at the request of the NASA Engineering and Safety Center Board to help assess the accuracy of the computations performed on the relatively complex D118-RPM-600_2-001 damage site. The rationale for this effort was to provide a simulation of an independent approximation of the cavity shape to confirm that the augmentation bump factors predicted by the standard rapid-analysis CFD approaches were not overly sensitive to the choice of simplified cavity geometry or simulation tool. Because of time constraints, only the LAURA CFD solver was applied to the alternative cavity geometry.

The resulting alternative cavity geometry is shown in Fig. 6. The cavity shape can be thought of as a hybrid between simplified cavity shapes 2 and 3. The MORPH utility was applied in polygon tracing mode to create the outline of the damage, so that the alternative cavity is oval-shaped rather than rectangular. The depth and angle of line segments below the OML were estimated from the point-cloud data shown in Fig. 4. The alternative cavity geometry does include an aft shelf, but it is smaller than that seen with simplified cavity 3, and the filler-bar region is larger than that modeled by simplified cavities 2 and 3. Limitations of MORPH preclude generation of a distinct cavity within a cavity, as modeled in the Ames simulation of simplified cavity 3. Consequently, the alternative cavity results cannot be used to estimate surface averages on the gap filler or plateau level of the real cavity. Rather, subjective judgments were made regarding the mapping of bump factors to the corresponding locations on simplified cavities 2 and 3.

As in other cavity grids generated for the STS-118 missions with MORPH, the cavity blocks connect smoothly to the baseline smooth-OML grid blocks. The construction is performed by generating precise vectors and projecting them a distance into the Orbiter from the OML until the desired depth and angle are obtained. The sideview, shown in Fig. 6, illustrates the attempt to mimic the dual

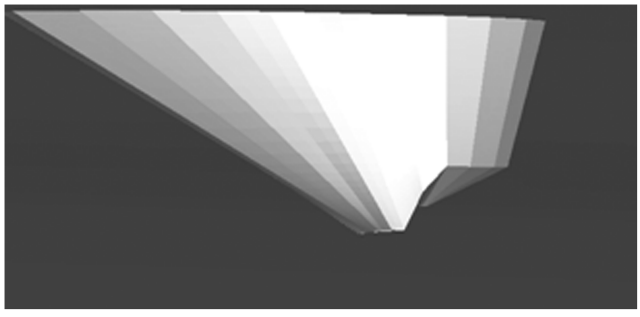

Fig. 6 Alternative cavity geometry sideview.

level of simplified cavity 3, but the floor and sidewalls have steeper angles due to limitations of the MORPH software. The surface grid was generated using the same metrics that were used with simplified cavity 2. The most forward part of the floor of the alternative cavity is approximately as deep as that of simplified cavity 2.

IV. Results

The objectives of the CFD analyses were to determine general flow features (recirculations, impingements, etc.) and convective heating-rate augmentation bump factors in and around the cavity. To meet the 18-h turnaround time requirement, the CFD effort was divided between the Ames and Langley CFD teams. The Langley team performed CFD calculations on the simplified geometry 2 and alternative cavity configurations using LAURA, and the Ames team computed the simplified cavity 3 cases with the DPLR flow solver.

A. General Flow Features

One of the objectives of the detailed CFD work was to gain insight into the flow features and physics within the cavity. Normalized enthalpy streamlines that illustrate the flow features inside the simplified cavity 3 geometry are shown in Fig. 7a, and the simplified cavity 2 streamlines are presented in Fig. 7b. The solutions for both cavities are at the Mach 23 condition. The streamlines are colored with contours of stagnation enthalpy normalized to the freestream stagnation enthalpy and are shown as ribbons so that flow rotation inside the cavity is visible. The flow direction in both figures is from left to right.

Based on the ratio of the cavity length to its depth, the D-118-RPM-600_2-001 cavity is classified as an open, or short, cavity. Typically, the length of an open cavity is not sufficient for the flow to impinge on the cavity floor. The simplified cavity 3 streamline traces in the upper half of Fig. 7 show the flow approaching from the left [1], passing over the cavity, and impinging on the upper portion of the back face of the cavity [2]. After hitting the backface, the flow is turned downward onto the backshelf. The flow then approaches the trench from the right [3]. Some of the flow passes over the trench and is turned upward to form the recirculating flow inside the open cavity [4]. The other portion of the flow impinges on the ramped wall [5] and is turned downward to form a secondary recirculation region inside the lower cavity [6]. Looking at the enthalpy ratio, which represents the energy of the streamlines and, therefore, the potential for heat transfer to the surface, it is apparent that the top portion of the backwall will experience a higher heat transfer rate, relative to other parts of the cavity. The flow that is turned downward and onto the backshelf is at a considerably lower energy level. This flow, which leaves the backshelf and is turned downward inside the lower cavity, is even cooler due to the expansion into that region. The flow pattern in simplified cavity 3 illustrates that the rear shelf shields the filler bar from direct flow impingement.

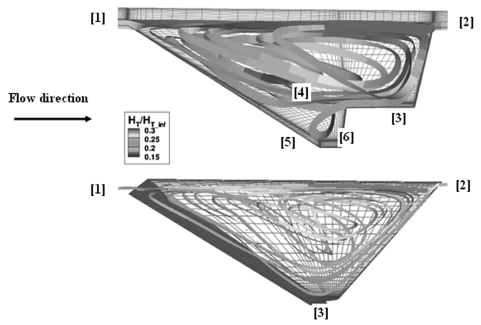

Fig. 7 Normalized enthalpy streamline traces, Mach 23: a) cavity 3 (DPLR), and b) cavity 2 (LAURA).

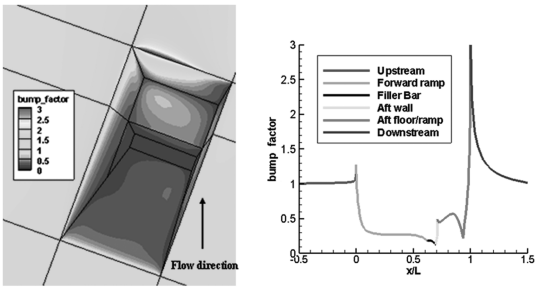

a) b)

Fig. 8 Mach 25 simplified cavity 3 DPLR results: a) surface-heating augmentation bump factors, and b) centerline bump factor profile.

In comparison, streamlines that impact on the ramped backface [2] of simplified cavity 2, shown in the bottom half of Fig. 7, impart less energy to the wall because the normal component to the velocity is relatively smaller due to the wall angle. The flow is turned downward and sweeps across the bottom of the cavity [3]. The normalized total enthalpy levels at the bottom of simplified cavity 2 are approximately equal to those on the backshelf of simplified cavity 3. Therefore, the heating levels on the bottom of simplified cavity 2 are expected to be higher than those at the bottom of simplified cavity 3, where the flow expands into the trench to form a cooler recirculation region. Because the alternative cavity geometry was similar to that of simplified cavity 2, its streamline traces (not shown) are likewise similar.

In summary, simplified cavity 3 shows a flowfield with two recirculating regions that yield a cooler flow on the cavity floor than either the simplified cavity 2 or alternative cavity geometries. Simplified cavity 3, however, has a higher heat transfer rate on the upper portion of the backwall than simplified cavity 2 due to the more vertical angle of the wall.

B. Heating Augmentation Bump Factors

Another objective of the CFD analysis was to compute heating augmentation bump factors on the surface of the cavity and compare these values against those generated by the engineering techniques that provide inputs to the thermal analysis models. The CFD bump factors are computed by dividing the local heating in and around the cavity by a reference heating rate value taken 0.5 in. upstream of the cavity. Bump factors for the Mach 25 simplified cavity 3 CFD solution are shown in Fig. 8a, where the black lines in the figures represent grid zonal boundaries. Because the location of the cavity is on a relatively flat section of the windward surface of the Orbiter, the heating rate remains relatively constant in the vicinity of the cavity, and the bump factor values are close to one. The flow direction is from the bottom edge of the figure to the top. A slight crossflow velocity component is indicated by the off-center hot spot along the rear edge of the cavity. The aft floor region of the cavity shows an elevated heating level, but the bump factors along the filler bar for simplified cavity 3 are relatively low with values ranging from about 0.2 to 0.3. The levels on the backshelf of the cavity range between 0.5 and 0.7.

The CFD bump factor profile down the centerline of the cavity at Mach 25 is presented in Fig. 8b. The results are shown as a function of normalized distance, where the cavity is situated between $0 < x/L < 1$ and the leading edge of the cavity is at $x/L = 0$. In Fig. 8b, the flow direction is from left to right. The filler-bar region (the primary area of interest) is the segment between $0.625 < x/L < 0.7$ and is represented by the black line on the profile. The filler-bar bump factors ranged from about 0.16 at Mach 25 to 0.26 at Mach 16.5. The centerline profiles for the other four Mach numbers computed are not shown but are quite similar.

The LAURA simplified cavity 2 bump factor surface contours for Mach 25 are shown in Fig. 9a. The black lines indicate the surface grid zonal boundaries, and they are different from the simplified cavity 3 zonal boundaries because the DPLR and LAURA grids used different topologies, and the cavity geometries themselves are different. The bump factor profile down the centerline of simplified cavity 2 is presented in Fig. 9b. Comparing the simplified cavity 2 and 3 surface bump factor contours, the bump factors along the filler

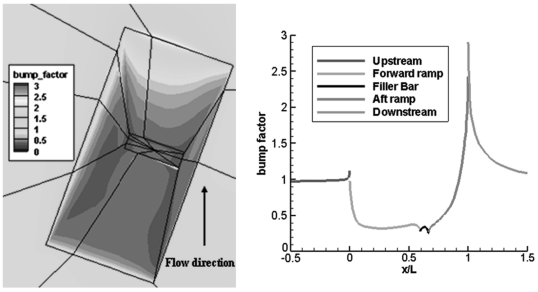

a) b)

Fig. 9 Mach 25 simplified cavity 2 LAURA results: a) surface-heating augmentation bump factors, and b) centerline bump factor profile.

bar are slightly higher and aft ramp regions are noticeably higher for simplified cavity 2 than they are for simplified cavity 3.

Because of time constraints during STS-118, a Mach 25 LAURA case was not completed for the alternative cavity geometry during STS-118, and so a direct comparison to the results in Figs. 8 and 9 is not available. However, a LAURA Mach 24 alternative cavity solution was computed, and the resulting surface bump factor contours are shown in Fig. 10a. With the alternative cavity geometry, the filler-bar region is no longer modeled as a short, rectangular region. Instead, the filler bar is represented by a larger, more complex shape, and the resulting filler-bar bump factors are higher than either the simplified cavity 2 or simplified cavity 3 results. The bump factor profile down the approximate center of the alternative cavity is shown in Fig. 10b.

The centerline bump factor profiles presented in Figs. 8–10 are overlaid for comparison in Fig. 11. As expected, in the filler-bar region between $0.625 < x/L < 0.7$, the simplified cavity 2 and alternative cavity solutions show higher heating augmentation bump

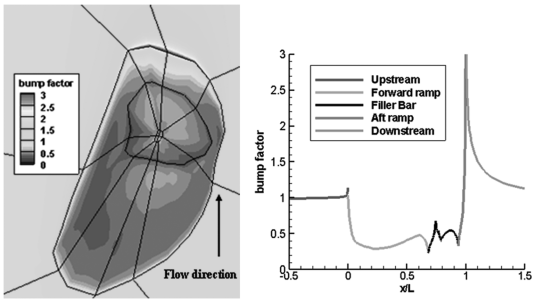

a) b)

Fig. 10 Mach 24 alternative cavity LAURA results: a) surface-heating augmentation bump factors, and b) centerline bump factor profile.

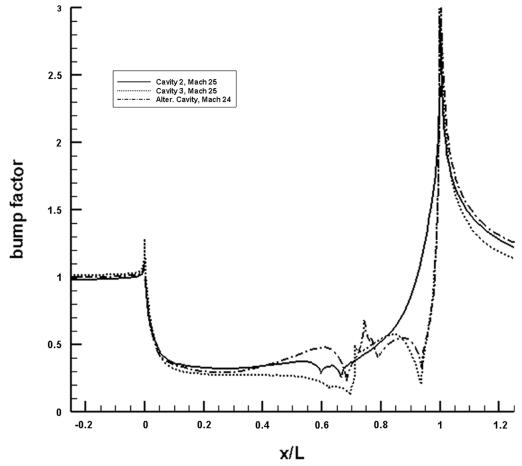

Fig. 11 Centerline bump factor profiles, Mach 24–25.

factors than were predicted with simplified cavity 3. Along the aft ramp region, the alternative cavity results are quite similar to the simplified cavity 3 solution.

Figures 8–11 show results for CFD computations at Mach 24 and 25. Although not shown in this paper, the surface contour plots and centerline profiles for the simplified cavity 2 and 3 computations at Mach numbers of 23, 20, 18, and 16.5 exhibited similar trends, namely higher bump factors along the filler bar and aft ramp for the simplified cavity 2 solutions than were seen in the simplified cavity 3 results.

As was stated previously, the heating rate bump factors used in the thermal model for trapezoidal shoebox-shaped cavities are primarily obtained from the CHT, which uses correlations derived from experimental data. The CFD flight-cavity results computed during STS-118 were used to corroborate the engineering data. A comparison was made between the CFD- and engineering-derived bump factors for the three CFD cavity geometries at the control points shown in Figs. 12a and 12b. In both figures, control points 3 and 4 are located on the surface of the filler bar.

The results of the comparison are shown in Table 2, which show the spanwise averge bump factors at the various control points. The CHT was run as is for simplified cavity 2, which has a trapezoidal shoebox shape. The engineering values listed in the table for simplified cavity 3 were not taken directly from the CHT, because it cannot directly model a cavity on top of a cavity. Instead two separate CHT analyses were performed to approximate the simplified cavity 3 geometry. The CFD values in Table 2 include an increment of 0.15 (corresponding to a 50% uncertainty estimate for the CFD previously obtained from comparisons with experimental data in [6]) to both the DPLR and LAURA results to account for the uncertainty level of open cavity CFD computations. For comparison, the CHT results have an uncertainty of up to 20% depending on the cavity dimensions and flow conditions [3]. The ranges in the CFD values listed in Table 2 reflect bump factor variations due to changes in freestream conditions shown in Table 1.

Overall, the CFD results are consistent with the engineering estimates for simplified cavity 3, generally overpredicting the CHT-based results. The largest discrepancy occurs at control point 7, which is not a critical element of the cavity-heating analysis. The other large discrepancy is at control point 8, which is a forward-facing sharp corner. CFD results are typically unreliable at forward-facing sharp corners due to a 1-D conduction assumption in the models, and CFD uncertainties at this type of geometry have not been established. Along the filler-bar floor at control points 3 and 4, the correlation between the engineering and CFD bump factors is quite close, with the CFD slightly overpredicting the engineering values.

The simplified cavity 2 and alternative cavity geometries were expected to yield more conservative (i.e., higher) heating bump factor values on the cavity floor than the simplified cavity 3 geometry. The values in the two right-hand columns of Table 2 confirm this expectation. The engineering values at control points 3 and 4 (along the filler bar) are at least twice as large for the simplified cavity 2 and alternative cavity geometries as they were for simplified cavity 3. The CFD values along the cavity floor for simplified cavity 2 were about 50% larger than were seen with simplified cavity 3. The CFD and engineering values for simplified cavity 2 are quite close at control point 3, whereas the CFD underpredicts the engineering values at control point 4. The alternative cavity flow structures agree most readily with the cavity 2 geometry, and the alternative cavity bump factors are, generally, more like the cavity 2 environments than they are like the cavity 3 environments.

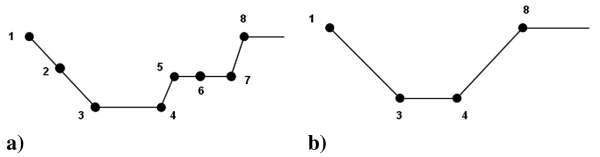

a) b)

Fig. 12 Schematic of bump factor comparison control points: a) simplified cavity 3, and b) simplified cavity 2 and alternative cavity.

Table 2 Comparison of engineering and CFD bump factors

Control point	Cavity 3, CHT	Cavity 3, DPLR	Cavity 2, CHT	Cavity 2, LAURA	Alternative cavity, LAURA
1	1.0	1.09–1.21	1.00	1.0	1.0
2	0.48	0.38–0.52	——	——	——
3	0.23	0.31–0.38	0.48	0.44–0.54	0.55
4	0.23	0.26–0.28	0.70	0.41–0.49	0.72
5	0.48	0.60–0.67	——	——	——
6	0.48/0.70	0.74–1.00	——	——	——
7	0.70	0.38–0.49	——	——	——
8	2.35	3.30–4.34	2.35	2.40–2.75	3.4

Table 3 Comparison of simplified cavity 2 bump factors (LAURA values are the first values in each column, DPLR values are in square brackets, percentage differences are in parentheses)

Mach number	Control point 1	Control point 3	Control point 4	Control point 8
25	1.0 [1.10] (10.0)	0.47 [0.41] (12.7)	0.44 [0.45] (2.2)	2.40 [2.74] (14.1)
23	1.0 [1.08] (8.0)	0.44 [0.48] (9.1)	0.41 [0.48] (17.0)	2.64 [2.65] (0.4)
20	1.0 [1.10] (10.0)	0.46 [0.42] (8.7)	0.41 [0.43] (4.9)	2.62 [2.58] (1.5)
18	1.0 [1.07] (7.0)	0.53 [0.48] (9.4)	0.47 [0.48] (2.1)	2.72 [2.64] (4.4)
16.5	1.0 [1.06] (6.0)	0.54 [0.52] (3.7)	0.49 [0.51] (4.1)	2.75 [2.59] (5.8)

C. Code-to-Code Comparison for Simplified Cavity 2

The CFD simulations performed during STS-118 were all computed using a single flow solver for each cavity geometry. The DPLR code was used for the simplified cavity 3 calculations, and the LAURA code was used to generate the simplified cavity 2 and alternative cavity solutions. After the completion of the STS-118 mission, the Ames procedures were used to perform calculations at 5 Mach numbers for the simplified cavity 2 geometry. As well as representing a code-to-code comparison of the CFD flow solvers, this additional work also provides a measure of the grid sensitivity of the solutions, because the LAURA and DPLR calculations used quite different grid topologies. Surface-heating bump factor contours for the Mach 25 solutions are shown in Fig. 13, and the two solutions are qualitatively similar.

A more quantitative assessment of the correlation between the LAURA and DPLR simplified cavity 2 computations can be obtained by examining the bump factor profiles taken down the center of the cavity as shown in Fig. 14. The filler-bar region is highlighted inside the dashed circle. The figure presents the Mach 25 results, and the correlation between the two solutions is quite close along the filler bar, along the aft ramp, and downstream of the cavity. There is some discrepancy along the forward ramp region, where the maximum percentage difference between the LAURA and DPLR bump factor values is about 18% at a location of approximately $x/L = 0.5$. Along the filler bar, which was the main area of interest for the CFD computations, the maximum difference between the CFD solutions is 7.6%. Although not shown, the other 4 Mach number cases showed similar correlation characteristics between the LAURA and DPLR solutions.

Floor-averaged bump factors (averaged in the spanwise direction) were computed for the DPLR solutions at the control points indicated in Fig. 12b. The DPLR values are compared against those from the LAURA simplified cavity 2 solutions in Table 3. The LAURA values are the first values in each column of the table and the DPLR values are the middle values in square brackets. Percentage differences

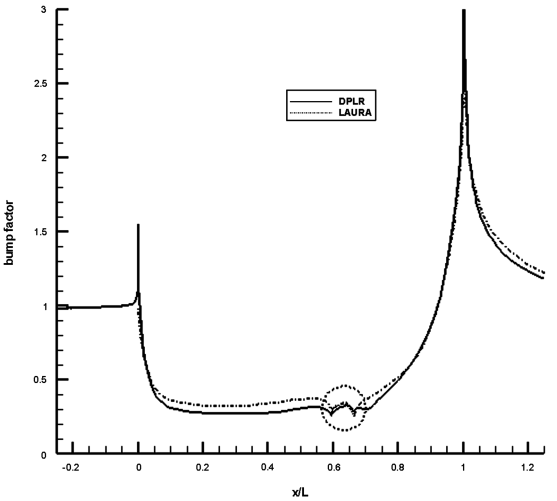

Fig. 14 Comparison of Mach 25 CFD bump factor profiles down the cavity 2 centerline.

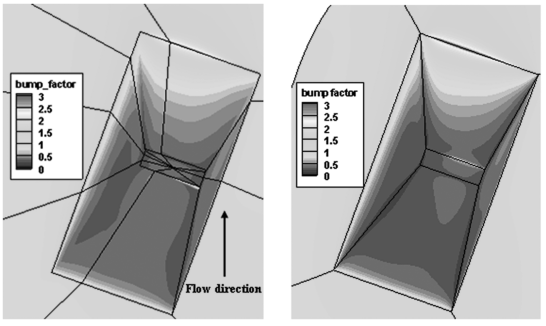

a) b)

Fig. 13 Comparison of Mach 25 cavity 2 surface bump factors: a) LAURA solution, and b) DPLR solution.

a) b)

Fig. 15 Comparison of damage site photos: a) postflight, and b) in-space.

between the CFD results are listed in parentheses. Considering that the two sets of CFD solutions were performed using different flow solvers on different grid topologies, there is a close correlation between the LAURA and DPLR floor-averaged values, with a maximum percentage difference of approximately 17% at the Mach 23 condition at the control point 4 location.

V. Conclusions

The CFD analysis performed on damage site D-118-RPM-600_2-001 was part of an integrated effort during STS-118 to determine if an EVA was required to repair the damage site. A total of 12 3-D real-gas local cavity CFD solutions were computed (including grid generation), postprocessed, and presented to the DAT in an 18-h period of time. Three different cavity geometries were investigated, which included two simplified shoebox-type cavities and an alternative, irregularly shaped geometry.

One of the objectives of the CFD analysis was to provide insight into the general flow features in and around the damage site. Normalized enthalpy streamline plots were prepared to illustrate these flow patterns. The simplified cavity 3 results showed a flowfield with two recirculating regions, which yielded a cooler flowfield on the cavity floor (i.e., filler bar) than for the simplified cavity 2 and alternative cavity geometries. Simplified cavity 3 showed, as expected, a higher heat transfer rate on the upper portion of the backwall than the simplified cavity 2 or alternative cavity geometries due to the more vertical angle of the simplified cavity 3 backwall.

The second objective of the detailed CFD calculations was to provide heating augmentation bump factors and compare them with the engineering values used in the thermal analysis models. As was indicated by the normalized enthalpy streamlines, the heating bump factors showed that the more traditional shoebox cavities of the simplified cavity 2 and alternative cavity geometries were more conservative in terms of heating augmentation bump factor on the filler bar than the cavity on top of a cavity geometry of simplified cavity 3. Generally, there was good correlation between the floor-averaged CFD bump factors and those obtained from the engineering methods.

Based in part on the detailed CFD solutions generated by the Ames and Langley CFD teams during STS-118 (as part of a much larger and more extensive DAT process that included thermal and structural analysis), it was decided by the MMT not to perform a spacewalk to repair the D-118-RPM-600_2-001 damage site but rather to fly Space Shuttle *Endeavour* back to Earth as is. The decision was not unanimous, and some engineers and managers argued for the repair option. The vehicle successfully reentered the Earth's atmosphere and landed on 21 August 2007. An image of the damage site taken during the postflight inspection of the vehicle is shown in Fig. 15a. Comparing it with the in-space damage site photo shown in Fig. 15b, it can be seen that the damage site did not enlarge during reentry, a result consistent with the DAT aerothermal, thermal, and structural predictions. Postflight inspection confirmed that the filler bar remained intact during reentry and no structural damage occurred in this area. Overall, the rapid analysis of the D-118-RPM-600_2-001 cavity highlights the capability of using high fidelity CFD simulations for real-time damage assessment during a shuttle mission.

Acknowledgments

The computational fluid dynamic analysis described in this paper is only one small piece of an extensive and well-integrated team that works diligently during shuttle missions to ensure that the crew and vehicle return safely. The entire damage assessment team, from the people who analyze the video imagery, to those who develop the computer aided three-dimensional interactive application models of the damage sites, to the analysts who determine the aerodynamic, thermal, and structural consequences of any thermal protection system damage that might be present, use their expertise to generate the best possible damage assessment information in the shortest possible time. The lessons of the Space Shuttle *Columbia* accident have been well learned by the hardworking people at NASA, Boeing, and United Space Alliance who are part of the damage assessment team.

References

[1] Columbia Accident Investigation Board Rept., Vol. 1, NASA, Aug. 2003.

[2] Campbell, C. H., Anderson, B., Bourland, G., Bouslog, S., Cassady, A., Horvath, T. J., Berry, S. A., Gnoffo, P. A., Wood, W. A., Reuther, J. J., Driver, D. M., Chao, D. C., Hyatt, J., and Picetti, D., "Orbiter Return to Flight Entry Aeroheating," AIAA Paper 2006-2917, June 2006.

[3] Hyatt, J., Wang, K. C., Everhart, J., Greene, F., Merski, R., Wood, B., Berger, K., Anderson, B., and Cassady, A., "The Cavity Heating Tool Version 3.0 Documentation," Boeing ATA-AH-TM-2006-035, March 2006.

[4] Tang, C., Saunders, D., Trumble, K., and Driver, D., "Rapid Aerothermal Simulations of Damage and Repair During a Space Shuttle Mission," AIAA Paper 2007-1783, April 2007.

[5] Pulsonetti, M. V., and Wood, W., "Computational Aerothermodynamic Assessment of Space Shuttle Orbiter Tile Damage: Open Cavities," AIAA Paper 2005-4679, June 2005.

[6] Palmer, G. E., Alter, S., Everhart, J., Wood, W., Driver, D., Brown, J., and Prabhu, R. K., "CFD Validation for Short and Long Cavity Flow Simulations," AIAA Paper 2007-4254, June 2007.

[7] Chawner, J. R., and Steinbrenner, J. P., "Automatic Structured Grid Generation Using Gridgen," NASA CP-3291, May 1995.

[8] Wright, M. J., Candler, G. V., and Bose, D., "Data-Parallel Line Relaxation Method for the Navier–Stokes Equations," *AIAA Journal*, Vol. 36, No. 9, 1998, pp. 1603–1609. doi:10.2514/2.586

[9] Gnoffo, P. A., "An Upwind-Biased, Point-Implicit Algorithm for Viscous, Compressible Perfect-Gas Flows," NASA TP-2953, Feb. 1990.

[10] Gnoffo, P. A., and Weilmuenster, K. J., "Multiblock Analysis for Shuttle Orbiter Re-Entry Heating from Mach 24 to Mach 12," AIAA Paper 93-2813, June 1993.

[11] Reuther, J. J., Brown, J. L., Prabhu, D. K., McDaniel, R., Saunders, D., and Palmer, G., "External Computational Aerothermodynamic Analysis of the Space Shuttle Orbiter at STS-107 Flight Conditions," AIAA Paper 2004-2281, June 2004.

[12] Fay, J. A., and Riddell, F. R., "Theory of Stagnation Point Heat Transfer in Dissociated Air," *Journal of Aeronautical Sciences* , Vol. 25, No. 2, 1958, pp. 73–86.

K. Wurster
Associate Editor